Available online at www.sciencedirect.com
ScienceDirect
Solar Energy xxx (2009) xxx–xxx
SOLAR ENERGY
www.elsevier.com/locate/solener

Solar radiation and shadow modelling with adaptive triangular meshes

G. Montero *, J.M. Escobar, E. Rodríguez, R. Montenegro

University Institute for Intelligent Systems and Numerical Applications in Engineering, University of Las Palmas de Gran Canaria, Campus Universitario de Tafira, 35017 Las Palmas de Gran Canaria, Spain

Received 25 March 2008; received in revised form 4 January 2009; accepted 7 January 2009

Communicated by: Associate editor Christian Gueymard

Abstract

In this work, we propose a numerical model for generating solar radiation maps with the use of 2-D adaptive meshes of triangles. These triangulations are constructed by using a refinement/derefinement procedure in accordance with the variations of terrain surface orography and albedo. This discretization has the advantage of defining the terrain characteristics with a minimum number of points, which reduces the computational cost for a given accuracy. Moreover, the model takes into account the effect of shadows for each time step, which are detected by analysing the crossing of the trajectory of the shaft of light with the triangles of the mesh. Thus, the solar radiation is first computed for clear-sky considering the different components of radiation, that is, beam, diffuse and reflected radiations. From the results of clear-sky radiation, the real-sky radiation is computed daily in terms of the clear-sky index. The maps of clear-sky index are obtained from a spatial interpolation of observational data that are available for each day at several points of the zone under consideration. Finally, the solar radiation maps of a month are calculated from the daily results. We illustrate the performance of the model with a numerical experiment related to an episode on the island of Gran Canaria.

Keywords: Solar radiation; Beam, diffuse and reflected radiations; Clear-sky; Real-sky; Shadows; Adaptive meshes

1. Introduction

Nowadays, the solar power is one of the world's most highly prized renewable energies. Many numerical models have been developed with the aim of maximizing solar radiation collection.

There are three groups of factors that determine the interaction of solar radiation with the earth's atmosphere and surface (see e.g., Šúri and Hofierka (2004, 2002)):

a. The earth's geometry, revolution and rotation (declination, latitude, solar hour angle).
b. Terrain (elevation, albedo, surface inclination and orientation, shadows).
c. Atmospheric attenuation (scattering, absorption) by
   c.1. Gases (air molecules, ozone, CO_2 and O_2).
   c.2. Solid and liquid particles (aerosols, including non-condensed water).
   c.3. Clouds (condensed water).

If we consider the three factors of atmospheric attenuation (c) in the model, it will produce real-sky radiation values. If we omit the cloud attenuation (c.3), clear-sky (cloudless) radiation values will be obtained.

The spatial modelling of solar radiation has been carried out over the last three decades in order to optimize the solar resource management. In general, and considering the type of basic data/approach, we find two main groups of spatial models. There are, on the one hand, those based on the study of data obtained from satellite observations (see e.g., Cogliani et al. (2008)), and, on the other, those based on the astrophysical, atmosphere physical and geometrical considerations. Among the latter group, we high-

* Corresponding author. Tel.: +34 928451923; fax: +34 928457402.
E-mail address: gustavo@dma.ulpgc.es (G. Montero).

0038-092X/$ - see front matter © 2009 Elsevier Ltd. All rights reserved.
doi:10.1016/j.solener.2009.01.004

light the works of Šúri and Hofierka (2004, 2002) regarding a GIS-based solar radiation model.

The purpose of this paper is the calculation of solar radiation on the terrain. The possible applications of these calculations are related to different fields. Solar radiation research is important not only in meteorology but also in forestry, agronomy, geography, medicine, etc. Solar radiation affects all physical, chemical and biological processes in the terrestrial ecosystem. For solar collectors, the application of our model is straightforward. It can determinate the terrain-induced shading on collectors, although currently it is not oriented to radiation computation on them. We should use the altimetry for shadow modelling and a fixed orientation and inclination of the collectors in order to calculate the solar radiation. The shadowing of a collector over another would not be considered by this model at the present form.

In this work, we propose some improvements to the model of Šúri and Hofierka (2004, 2002) related to the second factor (b) affecting the solar radiation. However, they can also be applied to other similar models for generating solar radiation maps. Specifically, we focus the study on the accurate definition of the terrain surface and on the produced shadows by using an adaptive mesh of triangles. Some previous studies on shadow detection are based on the geometrical considerations but they are too costly in processing time to apply in complex terrain (see e.g., Niewienda and Heidt (1996) and Zakšek et al. (2005)). First, the work of Niewienda et al. proposes to calculate the GSC (geometrical shading coefficient), the proportion of shaded area of an arbitrarily oriented surface surrounded by shading elements as a function of time and location. It focuses on the detection of shadow over local surfaces, buildings, objects, etc. Also, Zaksek et al. propose a solar radiation model based on the defining incidence angle by computing normal-to-the-surface tangent plane and direction of the Sun. Since they use a regular grid in their computations, the computational cost of this approach is higher than others using an adaptive discretization.

The methods of Dozier et al. (1981) and of Stewart (1998) calculate approximate horizons for each sample point of the terrain surface. They do not consider a solid surface and, thus, need a high density of sample points in order to obtain accurate results. In contrast, our approach uses a mesh representing a solid surface that actually casts shadows and so it is not as sensitive as the former to the density of sample points. The adaptive triangulation of the terrain allows the shadow distribution in a region to be obtained with reasonable precision at a low computational cost. Thus, we propose to introduce in this field the mesh refinement/derefinement techniques that have been widely used in other scientific problems (Winter et al., 1995; Ferragut et al., 1994; Montero et al., 2005, 2004). On the one hand, the refinement strategy increases the resolution of the mesh by subdividing a given triangle (*father*) into several subtriangles (*sons*). On the other hand, the derefinement, i.e., the elimination of mesh triangles, is the inverse procedure of the refinement. Specifically, this model includes the implementation of 4-T Rivara's refinement algorithm (Rivara, 1987) and derefinement algorithm (Plaza et al., 1996), developed by Ferragut et al. (1994).

In short, our adaptive model allows the refinement of the results of a GIS-based model that would have a high computational cost in accurate local area simulations. In addition, this model may be connected to a GIS tool as a local solver.

In Section 2, we develop the technique for generating the meshes adapted to topography and albedo. The resulting triangular mesh provides a discretization of the studied zone with greater density of points where there are more variations of altimetry and albedo. The procedure used for determining the shadows according to the solar hour angle and terrain characteristics is presented in Section 3. From the surface discretization and shadow distribution, we carry out the estimation of the solar radiation under clear-sky conditions, considering the beam, diffuse and reflected radiation. Then, the real-sky solar radiation is computed using available measures at a set of points. This aspect is described in Section 4. Section 5 is devoted to showing the results of a numerical experiment in the Canary Islands which illustrate the performance of this model. Finally, we present our conclusions and propose future research.

2. Construction of the terrain surface mesh

Orography and albedo are two essential variables to be included in a solar radiation model. If accurate information of the terrain orography and albedo is available, an adaptive procedure of mesh refinement/derefinement should be able to capture them simultaneously. This procedure has been carried out using two different derefinement parameters. Other approaches such as Delaunay triangulation or other more complex triangulation methods capable of adaptation to specific features (e.g., ridges, valley bottoms) and changing complexity of represented phenomena may be applied. Although all these methods may be valid for defining the initial mesh adapted to terrain orography and albedo, nested meshes are more efficient to transfer information along an evolution process (for example, shadow and radiation) from mesh to mesh, when the mesh changes from one step to another (for example, mesh adaption). In these processes, local adaption to shadow boundary and radiation gradient using refinement/derefinement of nested meshes would be preferable to remeshing.

The mesh generation process starts with the determination of nodes allocated on the terrain surface. Their distribution must be adapted to the orographic and albedo characteristics in order to minimize the number of required nodes for a given accuracy. The procedure first builds a sequence of nested meshes $\Gamma = \{\tau_1 < \tau_2 < \ldots < \tau_m\}$ from a regular triangulation τ_1 of the rectangular region under study, such that the level τ_j is obtained by a global refinement of the previous level τ_{j-1} with 4-T Rivara's algorithm (Rivara, 1987). Each triangle of level τ_{j-1} is divided into

Please cite this article in press as: Montero, G. et al., Solar radiation and shadow modelling with adaptive triangular meshes, Sol. Energy (2009), doi:10.1016/j.solener.2009.01.004

four subtriangles inserting a new node in the middle point of the edges and connecting the node inserted in the longer edge with the opposite vertex and with the other two new nodes. Thus, new nodes, edges and triangles that are defined as corresponding to level j appear in the mesh level τ_j. The number of levels m of the sequence is determined by the degree of discretization of the terrain, i.e., the diameter of the triangulation τ_m must be of the order of the spatial step of the digital map that we are using. In this way, we ensure that this regular mesh is able to capture all the orographic and albedo information by an interpolation of the heights and albedo in the nodes of the mesh.

Then, we define a new sequence $\Gamma' = \{\tau_1 < \tau'_2 < \ldots < \tau'_{m'}\}, m' \leqslant m$, by applying the derefinement algorithm (Ferragut et al., 1994; Plaza et al., 1996). In this step, two derefinement parameters ε_h and ε_a are introduced and they determine the accuracy of the approximation to terrain surface and albedo, respectively. The absolute difference between the height obtained in any point of the mesh $\tau'_{m'}$ and the corresponding exact height will be lower than ε_h. A similar condition is established for the albedo and ε_a. Finally, the derefinement algorithm (see Algorithm 1) uses all the information of the element and edges genealogy defined in the sequence. The derefinement condition simultaneously takes into account the requirements of both height and albedo. On the one hand, we consider the analysis of the absolute difference between the exact height (usually referring to an interpolated value from the digital map) of a node and the interpolation of the height corresponding to the two extreme nodes of its environment edge, i.e., the edge in which that node was inserted in the middle point during the refinement process. On the other hand, the same analysis is carried out with the albedo. If the first difference related to the height is lower than ε_h and the second difference related to the albedo is lower than ε_a, simultaneously, then the node may be eliminated, although in some cases it will have to be kept for reasons of conformity.

This type of meshes has been successfully used in other problems as a previous step to construct a three-dimensional mesh of tetrahedra (Montenegro et al., 2002a,b; Montero et al., 2003).

Algorithm 1. Derefinement algorithm.

INPUT: Sequence $\Gamma = \{\tau_1 < \tau_2 < \ldots < \tau_m\}$.
for $j = m$ to 2 **do** {Loop in the levels of Γ}
For each node corresponding to τ_j, the derefinement condition is evaluated, and the nodes and edges that may be eliminated are marked by using derefinement vectors.
The conformity of the new mesh level j is ensured minimizing the derefined region.
if any node corresponding to τ_j stands **then**
New node connections are defined for the new level j: τ_j^j.
The vectors of the genealogy of τ_j^j and τ_{j-1} are modified.
else
The current level j is eliminated from the structure vectors.
The vectors of the genealogy of τ_{j-1} are modified.
end if
The changes in the mesh are inherited by the subsequent meshes.
The structure vectors are compressed.
A new sequence of nested meshes Γ^j is obtained.
$\Gamma^j = \{\tau_1 < \tau_2 < \ldots < \tau_{j-1} < \tau_j^j < \ldots < \tau_{m_j}^j\}$.
It is the input in the next step of the loop.
end for
OUTPUT: derefined sequence $\Gamma' = \Gamma^2 = \{\tau_1 < \tau'_2 < \ldots < \tau'_{m'}\}$.

3. Detection of shadows

Geographical features appearing in complex terrains cast shadows that must be considered for an accurate estimation of the solar radiation on a surface. The procedure for detecting these shadows stands on a simple idea. Looking at the mesh from the sun, let us consider that a triangle is in shadow if we can find another triangle that totally or partially covers the former. To carry out this analysis, we construct a reference system x', y' and z', with z' in the direction of the beam radiation (see Fig. 1), and the mesh is projected on the plane $x'y'$ (see Fig. 2).

We have assumed that differences in the direction of beam radiation are negligible over the area under study, and, thus, the transformation is only done once since it is the same for each triangle. For larger areas, the shadow detection procedure should be modified since a different transformation would need to be applied at each triangle of the mesh.

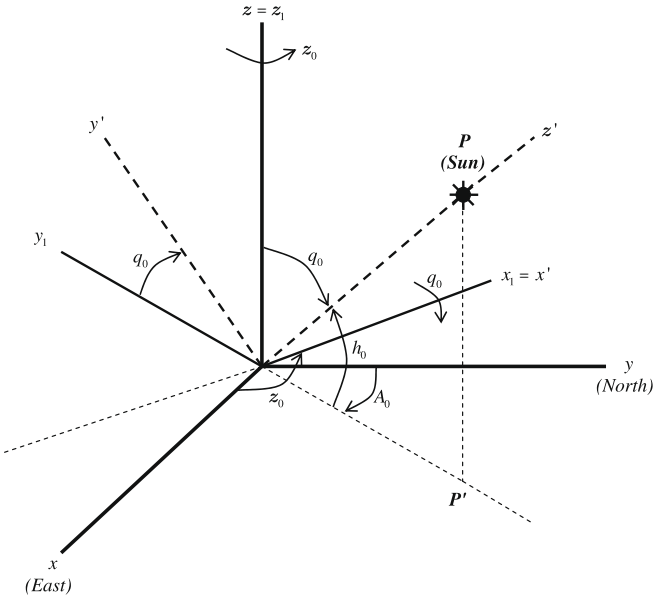

Fig. 1. Reference systems and Euler angles.

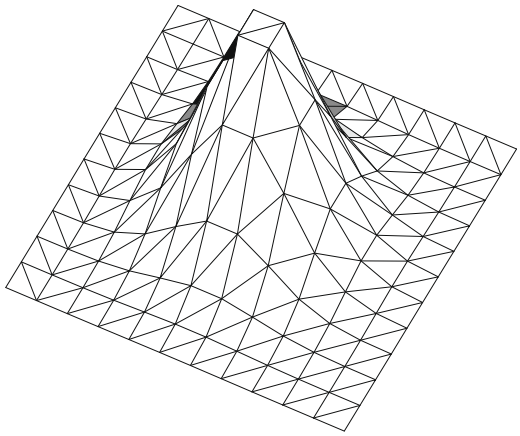

(a) Mesh viewed from the sun

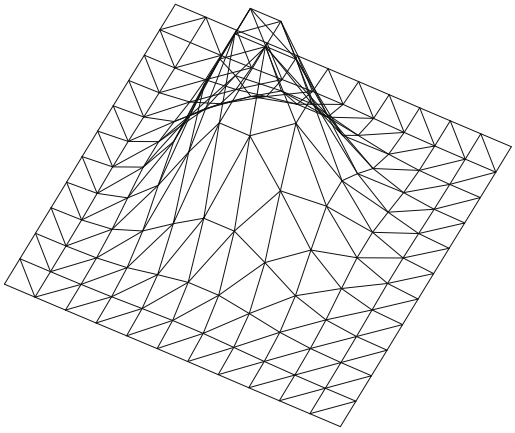

(b) Projected mesh

Fig. 2. Example of the shadow detection procedure.

We have taken into account that the sun position with respect to a horizontal surface is given by two coordinates, the solar altitude h_0 (an angle between the sun path and a horizontal surface) and the solar azimuth A_0 (horizontal angle between the sun and meridian) measured from north and clockwise (see Fig. 1), which are calculated as

$$\sin h_0 = \cos\varphi\cos\delta\cos T + \sin\varphi\sin\delta \tag{1}$$

$$\cos A_0' = \frac{\sin\varphi\cos\delta\cos T - \cos\varphi\sin\delta}{\sin h_0} \tag{2}$$

$$\text{if} \quad \sin T > 0, \quad A_0 = -A_0'$$

$$\text{if} \quad \sin T \leqslant 0, \quad A_0 = A_0'$$

T is the hour angle (rad) obtained from Eq. (5), φ the latitude in radians and δ the sun declination in radians obtained according to Gruter (1984),

$$\sin\delta = 0.3978\ \sin[j' - 1.4 + 0.0355\ \sin(j' - 0.0489)] \tag{3}$$

with j' being the day angle represented in radians as follows:

$$j' = \frac{2\pi j}{365.25} \tag{4}$$

Here j is the day number which varies from 1 on January 1st to 365 on December 31st. The hour angle T (rad) is calculated from the local solar time t expressed in decimal hours on the 24 h clock as

$$T = \frac{\pi}{12}(t - 12) \tag{5}$$

The vector that defines the direction of solar beam is (Niewienda and Heidt, 1996)

$$v_{sol} = \begin{pmatrix} \cos h_0\ \sin A_0 \\ \cos h_0\ \cos A_0 \\ \sin h_0 \end{pmatrix}$$

Then, the transformation to x', y', z' is carried out by means of matrix,

$$K = \begin{pmatrix} \cos z_0 & \sin z_0 & 0 \\ -\cos q_0\ \sin z_0 & \cos q_0\ \cos z_0 & \sin q_0 \\ \sin q_0\ \sin z_0 & -\cos z_0\ \sin q_0 & \cos q_0 \end{pmatrix}$$

where

$$z_0 = \pi - A_0 \tag{6}$$

$$q_0 = \pi/2 - h_0 \tag{7}$$

z_0 and q_0 being Euler angles associated to the transformation (see Fig. 1).

In practice, for each triangle of the surface mesh we compute two angles, the azimuth A_N (angle between the horizontal normal projection and East), and γ_N (angle between the normal to the triangle and the horizontal plane). The solar incidence angle δ_{exp} is then computed for each triangle (Krcho, 1990; Jenčo, 1992),

$$\sin\delta_{exp} = \cos\varphi'\cos\delta\cos(T - \lambda') + \sin\varphi'\sin\delta \tag{8}$$

where

$$\sin\varphi' = -\cos\varphi\sin\gamma_N\cos A_N + \sin\varphi\cos\gamma_N \tag{9}$$

$$\tan\lambda' = -\frac{\sin\gamma_N\sin A_N}{\sin\varphi\sin\gamma_N\cos A_N + \cos\varphi\cos\gamma_N} \tag{10}$$

Thus, we have assumed a constant irradiance on all the points of a given triangle.

Then, we check for each triangle Δ of the mesh, if there is another Δ' that intersects Δ and is in front of it, i.e., the z' coordinate of the intersection point with Δ' is greater than that with Δ.

The analysis of the intersection between triangles involves a high computational cost. For this reason, we have substituted the triangle that is to be studied with a small number of inner points. In this case, we have considered four warning points whose area coordinates, referenced to the master element with vertices (0,0), (1,0) and (0,1) of Fig. 3, are (1/3,1/6,1/2), (1/6,1/3,1/2), (2/3,1/6,1/6) and (1/6,2/3,1/6) (the geometrical centres of 4-T Rivara's subtriangles). We have used a rectangular grid in order to

Please cite this article in press as: Montero, G. et al., Solar radiation and shadow modelling with adaptive triangular meshes, Sol. Energy (2009), doi:10.1016/j.solener.2009.01.004

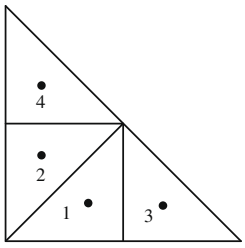

Fig. 3. Reference triangle.

classify the triangles in the mesh, which allows a fast search of the cast shadows over the warning points.

We assign a different level of lighting or shade to each triangle of the mesh depending on the number of warning points that lie inside other triangles. Specifically, a triangle Δ will have an associated lighting factor,

$$L_f = \frac{4-i}{4} \tag{11}$$

with $i = 0, 1, 2, 3, 4$ being the number of warning points inside other triangles that are in front of Δ. Clearly, L_f is a quantity between 0 and 1. This factor is used below in the estimation of beam and diffuse irradiances.

In short, the code for computing the shadows calculates the sun beam direction from the local hour, the time equation and the date, projects the mesh on the plane $x'y'$ and sweeps the triangles in order to obtain their lighting factors. Fig. 4a–d illustrate the shadows on a coarse triangulation of a simple surface for different times of a selected day (from 12:00 to 18:00 h of April, 15), from white (lighted) to black (shadowed) triangles.

This triangular network that was optimized for albedo and terrain variability may lack the capability to hold detailed (spatial variability) information about shadowing. This is the case when shadows from mountains are cast to the flat areas with sparse triangulation. In effect, our mesh is not currently adapted to the shadows. It is a fast approximation that has taken into account the main effect of orography and albedo on the shadow detection in the studied zone (we are able to define the shadow boundary). So we work with a fixed mesh for each time step. With an adaptive mesh we can capture such a boundary line. Other strategies may be applied, for example, using a different adaptive mesh for each time step. The proposed local refinement/derefinement algorithm may be useful for approximating the shadow boundaries. Of course, such an increase in accuracy entails an increase in the computational cost.

4. Solar radiation modelling

This solar radiation model is based on the work of Šúri and Hofierka (2004, 2002). We have proposed both the use of adaptive meshes for surface discretization and a new method for detecting the shadows over each triangle of the surface. We first calculate the solar radiation under the assumption of clear-sky for all the triangles of the mesh, taking into account the lighting factor of each triangle. Next, these solar radiation values are corrected for a real-sky by using the available data of the measurement stations. This procedure is carried out for each time step throughout an episode. Finally, the total solar radiation

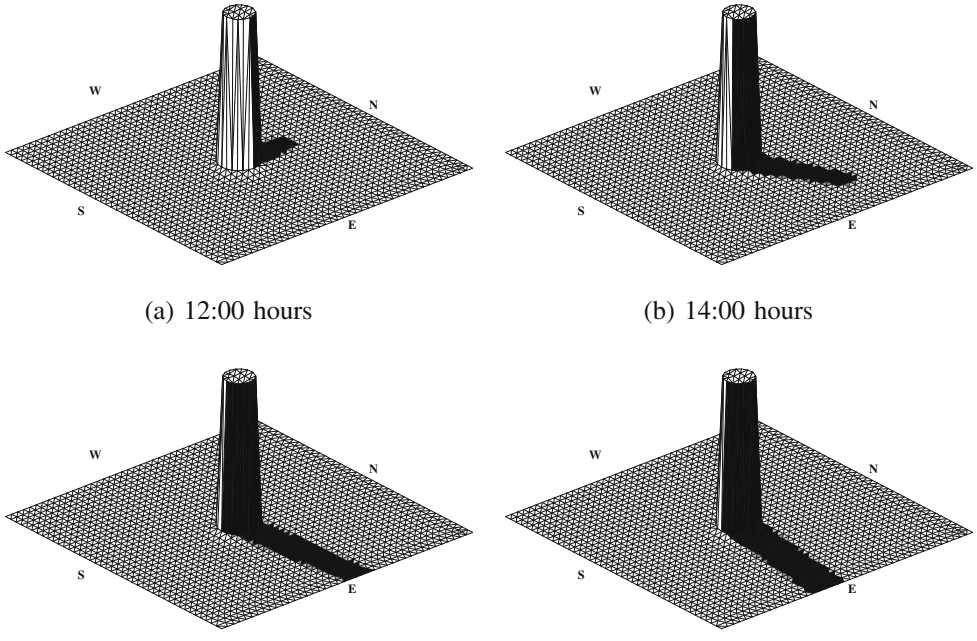

(a) 12:00 hours (b) 14:00 hours

(c) 16:00 hours (d) 18:00 hours

Fig. 4. Shadow evolution on a simple surface (April, 15). (a) $A_0 = 180°$, $h_0 = 71.68°$, (b) $A_0 = -117.10°$, $h_0 = 56.39°$, (c) $A_0 = -95.50°$, $h_0 = 30.97°$, (d) $A_0 = -81.35°$, $h_0 = 4.59°$.

Please cite this article in press as: Montero, G. et al., Solar radiation and shadow modelling with adaptive triangular meshes, Sol. Energy (2009), doi:10.1016/j.solener.2009.01.004

is obtained by integrating all the instantaneous values in each triangle.

4.1. Solar radiation equations for clear-sky

The global solar irradiance that comes into contact with the earth's surface comprises three different components: beam, diffuse and reflected irradiances. The first is partially attenuated by the atmosphere, is not reflected or scattered and reaches the surface directly. It is characterized by projecting sharp shadows of opaque objects. The second is the scattered irradiance that reaches the terrain surface. This irradiance goes in all directions and produces no shadows of the inserted opaque objects. Although this energy can be approximately the 15% of the global radiation on sunny days; however, on overcast days when the beam irradiance is very low, diffuse irradiance reaches a higher percentage. Finally, the last type of irradiance corresponds to that reflected from the surface onto an inclined receiver. The values of this irradiance for inclined surfaces depend on the albedo of the ground.

4.1.1. Beam radiation

The beam irradiance (or solar constant I_0) is 1367 (W/m^2) outside the atmosphere at the mean solar distance (Page, 1986). A correction factor ϵ is applied for calculation of the extraterrestrial irradiance $G_{(0)}$ normal to the solar beam, since the earth's orbit is lightly eccentric and the sun–earth distance varies slightly throughout the year.

$$G_0 = I_0\epsilon \tag{12}$$

where $\epsilon = 1 + 0.03344\ \cos(j' - 0.048869)$, with j' being the day angle; see Eq. (4). The beam irradiance normal to the solar beam B_{0c} (W/m^2) is attenuated by the cloudless atmosphere, and calculated as follows:

$$B_{0c} = G_0\ exp\{-0.8662T_{LK}m\delta_R(m)\} \tag{13}$$

The term $0.8662T_{LK}$ is the air mass 2 Linke atmospheric turbidity factor [dimensionless] corrected by Kasten (1996). The parameter m in (13) is the relative optical air mass calculated using the formula (Kasten and Young, 1989),

$$m = \frac{p/p_0}{\sin h_0^{ref} + 0.50572(h_0^{ref} + 6.07995)^{-1.6364}} \tag{14}$$

where h_0^{ref} is the solar altitude in degrees corrected by the atmospheric refraction component Δh_0^{ref},

$$\Delta h_0^{ref} = 0.061359\frac{0.1594 + 1.123h_0 + 0.065656h_0^2}{1 + 28.9344h_0 + 277.397h_0^2}$$
$$h_0^{ref} = \Delta h_0^{ref} + h_0 \tag{15}$$

and p/p_0 is a correction for a given elevation z expressed in metres,

$$p/p_0 = exp(-z/8434.5) \tag{16}$$

The parameter $\delta_R(m)$ is the Rayleigh optical thickness at air mass m that has been obtained for $m \leqslant 20$ with (Kasten, 1996)

$$\delta_R(m) = (k_0 + k_1m + k_2m^2 + k_3m^3 + k_4m^4)^{-1} \tag{17}$$

with $k_0 = 6.6296$, $k_1 = 1.7513$, $k_2 = -0.1202$, $k_3 = 0.0065$, $k_4 = -0.00013$.

For $m > 20$,

$$\delta_R(m) = (10.4156 + 0.718m)^{-1} \tag{18}$$

So, the beam irradiance on a horizontal surface B_{hc} becomes

$$B_{hc} = B_{0c}\ L_f\ \sin h_0 \tag{19}$$

where h_0 is the solar altitude angle, and L_f the lighting factor that corrects the beam irradiance as the surface is sunlit or shadowed. Then the beam irradiance on an inclined surface B_{ic} is obtained as

$$B_{ic} = B_{0c}L_f \sin\delta_{exp} \tag{20}$$

where δ_{exp} is the solar incidence angle measured between the sun beam direction and its projection on an inclined surface. Note that, for horizontal surfaces, δ_{exp} coincides with h_0.

4.1.2. Diffuse radiation

The estimation of the diffuse component in sunlit or shadowed horizontal surfaces D_{hc}(W/m^2) is carried out using the equation,

$$D_{hc} = G_0T_n(T_{LK})F_d(h_0) \tag{21}$$

where D_{hc} is a function of the diffuse transmission T_n which only depends on the Linke turbidity factor T_{LK} and on a function F_d depending on the solar altitude h_0 (Scharmer and Greif, 2000).

The calculation of the transmission function $T_n(T_{LK})$ is carried out using the second order polynomial,

$$T_n(T_{LK}) = -0.015843 + 0.030543T_{LK} + 0.0003797T_{LK}^2 \tag{22}$$

Moreover, the solar altitude function is

$$F_d(h_0) = A_1 + A_2\sin h_0 + A_3\sin^2 h_0 \tag{23}$$

where the values of A_1, A_2 and A_3 depend only on the turbidity T_{LK} and defined as

$$\begin{aligned} A_1' &= 0.26463 - 0.061581T_{LK} + 0.0031408T_{LK}^2 \\ A_1 &= \tfrac{0.0022}{T_n(T_{LK})} \quad \text{if } A_1'T_n(T_{LK}) < 0.0022 \\ A_1 &= A_1' \qquad \text{if } A_1'T_n(T_{LK}) \geqslant 0.0022 \\ A_2 &= 2.04020 + 0.018945T_{LK} - 0.011161T_{LK}^2 \\ A_3 &= -1.3025 + 0.039231T_{LK} + 0.0085079T_{LK}^2 \end{aligned} \tag{24}$$

On the other hand, the procedure for obtaining the clear-sky diffuse irradiance on an inclined surface D_{ic}(W/m_2) considers both sunlit and shadowed surfaces (see Section

3) following the equations proposed in Muneer (1990). For sunlit surfaces ($L_f = 1$) the equations are

If $h_0 \geqslant 0.1$ radians

$$D_{ic} = D_{hc}\left(F(\gamma_N)(1-K_b) + K_b\frac{\sin\delta_{exp}}{\sin h_0}\right) \tag{25}$$

If $h_0 < 0.1$ radians

$$D_{ic} = D_{hc}[F(\gamma_N)(1-K_b) + (K_b \sin\gamma_N \cos A_{LN})/(0.1 - 0.008h_0)] \tag{26}$$

where $A^*_{LN} = A_0 - A_N$

if $-\pi \leqslant A^*_{LN} \leqslant \pi$ then $A_{LN} = A^*_{LN}$
if $A^*_{LN} > \pi$ then $A_{LN} = A^*_{LN} - 2\pi$
if $A^*_{LN} < -\pi$ then $A_{LN} = A^*_{LN} + 2\pi$

For shadowed surfaces ($L_f < 1$).

$$D_{ic} = D_{hc}F(\gamma_N) \tag{27}$$

where $F(\gamma_N)$ is a function defined for the diffuse sky irradiance that may be computed as

$$F(\gamma_N) = r_i(\gamma_N) + N\left(\sin\gamma_N - \gamma_N\cos\gamma_N - \pi\sin^2\frac{\gamma_N}{2}\right) \tag{28}$$

γ_N being the inclination angle of the surface (rad) and $r_i(\gamma_N)$ a fraction of the sky dome viewed by an inclined surface,

$$r_i(\gamma_N) = (1+\cos\gamma_N)/2 \tag{29}$$

The value of N for shadowed surfaces is 0.25227, while for sunlit surfaces under clear sky, it is defined as

$$N = 0.00263 - 0.712K_b - 0.6883K_b^2 \tag{30}$$

K_b is a proportion between beam irradiance and extraterrestrial solar irradiance on a horizontal surface,

$$K_b = B_{hc}/G_{0h} \tag{31}$$

where

$$G_{0h} = G_0 \sin h_0 \tag{32}$$

4.1.3. Reflected radiation

Finally, the ground reflected irradiance under clear sky for inclined surfaces (R_i) is assumed to be proportional to the global horizontal irradiance G_{hc}, to the mean ground albedo ρ_g and a fraction of the ground viewed by an inclined surface $r_g(\gamma_N)$ (Muneer, 1997).

$$R_i = \rho_g G_{hc} r_g(\gamma_N) \tag{33}$$

where

$$r_g(\gamma_N) = (1-\cos\gamma_N)/2 \tag{34}$$

$$G_{hc} = B_{hc} + D_{hc} \tag{35}$$

In effect, this is a simplified model that includes the reflected radiation effect considering a horizontal surrounding terrain. A study of the effect of sloped surfaces on the reflected radiation would involve taking into account the reflection produced by all the triangles surrounding a triangle, which would lead to a high computational cost. Moreover, the contribution of the reflected component in the global radiation is generally less significant than other components.

4.2. Solar radiation under real-sky

The radiation for real-sky is obtained from the clear-sky radiation by applying a parameterization factor related to the cloud cover. Thus, the values of global radiation on a horizontal surface for real-sky conditions G_h are calculated as a correction of those of clear-sky G_{hc} with the clear-sky index k_c,

$$G_h = G_{hc}k_c \tag{36}$$

The index k_c represents the atmospheric transmission expressed as a ratio between the global radiation under real- and clear-sky conditions. If some measures of global radiation G_{hs} are available at different measurement stations, the value of the clear-sky index at each of these points may be computed as

$$k_c = G_{hs}/G_{hc} \tag{37}$$

Then k_c may be interpolated in the entire zone that is being studied. A simple formula that has also been used in other environmental problems defined on complex orography (see e.g., Montero et al. (1998)) is applied,

$$k_c = \varepsilon\frac{\sum_{n=1}^{N}\frac{k_{cn}}{d_n^2}}{\sum_{n=1}^{N}\frac{1}{d_n^2}} + (1-\varepsilon)\frac{\sum_{n=1}^{N}\frac{k_{cn}}{|\Delta h_n|}}{\sum_{n=1}^{N}\frac{1}{|\Delta h_n|}} \tag{38}$$

where k_c corresponds to the clear-sky index at each point of the mesh, k_{cn} is the clear-sky index obtained at the measurement stations, N is the number of stations used in the interpolation, d_n is the horizontal distance and $|\Delta h_n|$ is the difference in height between station n and the studied point, respectively, and ε is a parameter between 0 and 1. In problems with regular orography or in two-dimensional analyses, we choose high values of ε. However, for complex terrains, lower values of ε are a better choice. Thus, since in practice the studied regions often present both regular and irregular zones, an intermediate value of ε is more suitable. We have to include the case where the studied point coincides with a measurement station. In such cases, Eq. (38) is not continuous. The continuity is ensured if we assume the measured value at these points. Other versions of these classic weighting functions have been studied in the solar radiation problem in Şen and Şahin (2001). To calculate the value of B_h and D_h under real sky, a similar procedure may be applied from experimental measures.

5. Numerical experiments

The studied case corresponds to the island of Gran Canaria, which is one of the Canary Islands in the Atlantic Ocean at 28.06° latitude and −15.25° longitude. The UTM coordinates (metres) that define the corners of the consid-

Please cite this article in press as: Montero, G. et al., Solar radiation and shadow modelling with adaptive triangular meshes, Sol. Energy (2009), doi:10.1016/j.solener.2009.01.004

ered rectangular domain including the island are (417025, 3061825) and (466475, 3117475), respectively.

In order to calculate the reflected radiation, variable albedo in the region has been considered. Fig. 5 shows the albedo map of Gran Canaria. Albedo map was derived from a given map of different types of land use in Gran Canaria Island available in Infrastructure of Spatial Data of Spain, Consejo Superior Geográfico. In such maps, 85 types of land use in Spain are currently recorded. However, there are fewer types of land use (about 11) on Gran Canaria. From this map, we associate the types of land use to albedo values, based on the standard albedo tables found in the literature. In this simulation, the albedo of the zone varies from 0.05 (Macaronesic laurisilva) to 0.6 (Salt mine).

In general, the Canary Islands are characterized by complex terrains with high peaks in relative short surfaces. The topography of Gran Canaria is represented in Fig. 6, with a maximum height approximately of 1940 m. First, we construct a mesh of triangles that is adapted to the geographical characteristics of the terrain by using a refinement/derefinement procedure. In this solar radiation simulation, such refinement/derefinement procedure takes into account elevation and albedo maps, simultaneously. In this respect, the greater the number of variations of topography and albedo that are produced, the greater the required concentration of points will be. For this purpose, height and albedo must be known at each point of the mesh and, thus, they have to be interpolated from elevation and albedo mappings, respectively. This allows us to work with triangles from a few kilometres (e.g., on the sea) to a few metres (e.g., on the steep slopes) of edge length. We used $\varepsilon_h = 130$ and $\varepsilon_a = 0.08$, so that a mesh with 5866 nodes and 11683 triangles was built. This mesh is represented in Fig. 7.

The selected episode comprises the period from September 1st 2006, until May 31st 2007, for which each month is independently analysed. In particular, we present the graphical results for December as example. Beam, diffuse and reflected radiations are estimated each hour with the equations presented in Section 4. However, a step prior to the computation of the beam radiation is to calculate the shadow distribution on the mesh. This means that also the shadow detection procedure must also be run every hour from sunrise to sunset.

One additional datum required to calculate the diffuse radiation is the Linke turbidity factor. For example, it can be obtained online from the SoDa Service (2004–2007) for each month. On Gran Canaria it is 3.3, 3.2, 2.9, 2.7, 2.4, 2.4, 2.8, 3.0, 3.3 from September to May, respectively. Here, the use of hourly T_{LK} values would have

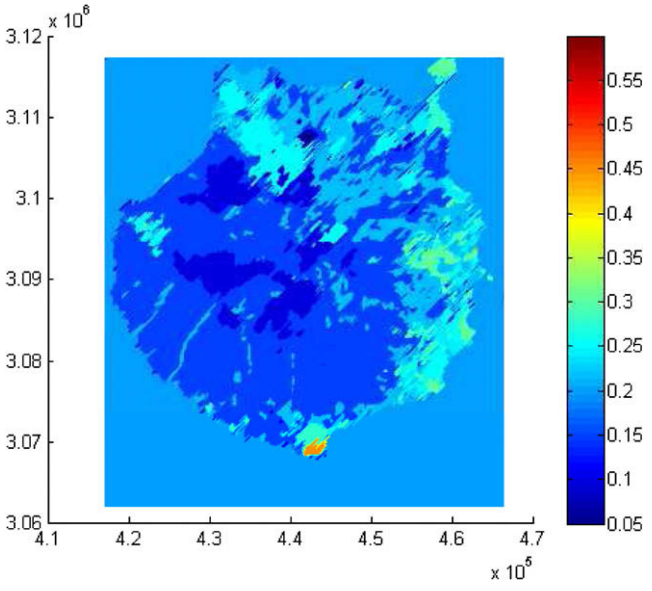

Fig. 5. Albedo map of Gran Canaria Island.

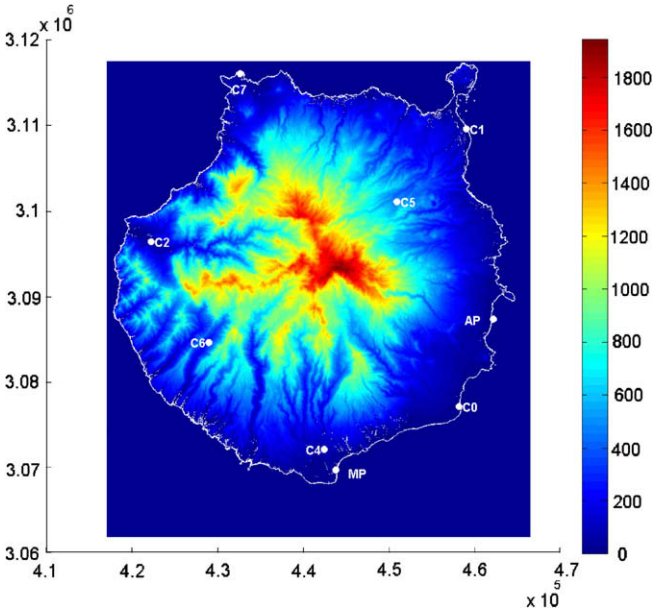

Fig. 6. Elevation map of Gran Canaria Island.

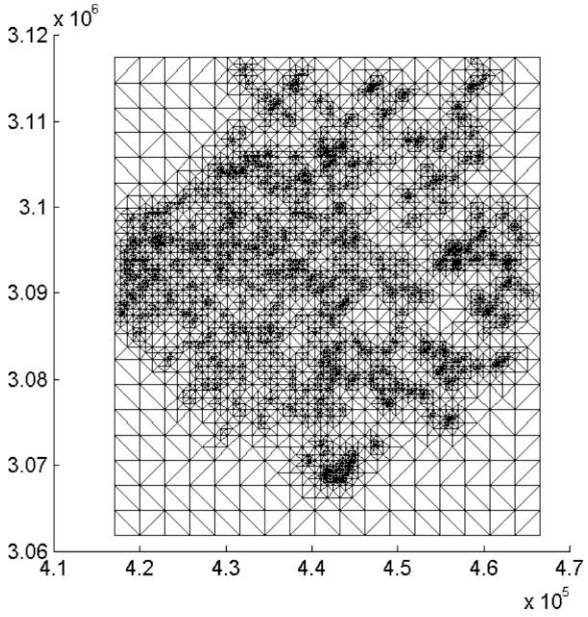

Fig. 7. Triangular mesh adapted to topography and albedo.

Please cite this article in press as: Montero, G. et al., Solar radiation and shadow modelling with adaptive triangular meshes, Sol. Energy (2009), doi:10.1016/j.solener.2009.01.004

Table 1
Geolocation of different sites on Gran Canaria Island. Beside latitude, longitude and height (m) of each station place, the corresponding description of village is provided.

Island	Site	Latitude	Longitude	Height
Pozo Izquierdo	C0	27.8175 N	15.4244 W	47
Las Palmas de G. C.	C1	28.1108 N	15.4169 W	17
La Aldea de San Nicolás	C2	27.9901 N	15.7907 W	197
San Fernando de M.	C4	27.7716 N	15.5841 W	265
Santa Brígida	C5	28.0337 N	15.4991 W	525
Mogán (village)	C6	27.8839 N	15.7216 W	300
Sardina de Gáldar	C7	28.1681 N	15.6865 W	40
Airport	AP	27.9325 N	15.3897 W	26
Maspalomas	MP	27.7500 N	15.5667 W	25

been more appropriate. However, the available data led us to simplify this aspect in the experiments. This problem has been pointed out by other authors. For example, Šúri and Hofierka (2004) applied their model with monthly data and they remarked that the calculus of T_{LK} values is critical. Some other authors have researched on the computation of the T_{LK} parameter at any given site and at the appropriate time interval from experimental data of solar radiation in different ways (Cucumo et al., 2000; Diabaté et al., 2003; Zakey et al., 2004).

Then, for each day, the clear-sky global radiation is computed hourly as the sum of the three components. We have used Simpson formula to integrate these data numerically in order to obtain the daily radiations. Although the time step used was 1 h, it can be reduced or increased, depending on the computational requirements.

We consider nine measurement stations that were available in the Island throughout the studied episode. Table 1 includes their locations. The radiation data of the first seven stations (C0, C1, C2, C4, C5, C6 and C7) have been provided by the Canary Islands Technological Institute (ITC) for October, November and December 2006 (Kuhlemann et al., 2005). The information of the last two stations, one in the region of the Airport (AP) and another in Maspalomas (MP) (see Fig. 6), was obtained from the Spanish National Meteorological Institute (INM) for the whole episode. We should add that station C3 referenced in Kuhlemann et al. (2005) is very close to C4 and MP and so it has not been included in this study.

The daily data of these stations have been used to obtain the corresponding real-sky global radiation from clear-sky results with $\varepsilon = 0.5$; see Section 4.2. Here, K_c was calculated as the daily mean value, since the available observa-

Table 2
Average and maximum beam, diffuse, reflected clear-sky radiations in December 2006. Also clear-sky and real-sky global radiations are included. All of them are represented in MJ/m^2 per day.

Day	Clear-sky								Real-sky	
	Beam rad.		Diffuse rad.		Reflected rad.		Global rad.		Global rad.	
	Aver.	Max.	Aver.	Max.	Aver.	Max.	Aver.	Max.	Aver.	Max.
1	12.44	23.48	2.52	3.77	0.06	0.73	15.02	27.46	12.27	22.51
2	12.37	23.44	2.52	3.77	0.06	0.73	14.95	27.43	11.56	21.10
3	12.31	23.41	2.51	3.77	0.06	0.72	14.88	27.40	10.30	19.56
4	12.25	23.38	2.51	3.78	0.06	0.72	14.82	27.37	10.91	20.16
5	12.19	23.35	2.50	3.78	0.06	0.72	14.75	27.34	12.32	22.74
6	12.14	23.33	2.50	3.78	0.06	0.72	14.70	27.31	9.13	18.89
7	12.09	23.30	2.50	3.78	0.06	0.70	14.64	27.28	12.13	22.57
8	12.04	23.28	2.49	3.78	0.06	0.69	14.59	27.26	9.91	19.34
9	12.00	23.25	2.48	3.78	0.06	0.69	14.54	27.24	8.39	15.86
10	11.96	23.23	2.48	3.78	0.06	0.69	14.50	27.22	9.49	17.66
11	11.92	23.21	2.48	3.78	0.06	0.69	14.46	27.20	7.88	15.09
12	11.89	23.19	2.48	3.78	0.06	0.69	14.42	27.18	9.20	17.21
13	11.86	23.18	2.47	3.78	0.06	0.69	14.39	27.16	9.55	18.58
14	11.83	23.16	2.47	3.78	0.06	0.68	14.36	27.15	8.97	17.41
15	11.80	23.15	2.47	3.78	0.06	0.68	14.33	27.14	11.45	21.88
16	11.78	23.14	2.47	3.79	0.06	0.68	14.31	27.13	11.64	22.18
17	11.77	23.13	2.47	3.79	0.06	0.68	14.29	27.12	9.97	19.02
18	11.75	23.13	2.47	3.79	0.06	0.68	14.28	27.11	4.52	8.62
19	11.74	23.13	2.46	3.79	0.06	0.68	14.27	27.11	10.72	20.43
20	11.74	23.12	2.46	3.79	0.06	0.68	14.26	27.11	10.55	20.12
21	11.73	23.12	2.46	3.79	0.06	0.68	14.26	27.11	8.39	16.15
22	11.73	23.13	2.46	3.79	0.06	0.68	14.26	27.11	8.91	17.12
23	11.74	23.13	2.46	3.79	0.06	0.68	14.26	27.12	5.85	14.12
24	11.75	23.14	2.47	3.79	0.06	0.68	14.27	27.12	11.82	22.36
25	11.76	23.14	2.47	3.79	0.06	0.68	14.28	27.13	10.17	19.41
26	11.77	23.15	2.47	3.79	0.06	0.68	14.30	27.14	11.65	22.38
27	11.79	23.17	2.47	3.79	0.06	0.68	14.32	27.16	12.09	23.04
28	11.81	23.18	2.47	3.79	0.06	0.68	14.34	27.17	9.27	17.53
29	11.84	23.20	2.47	3.79	0.06	0.69	14.37	27.19	11.77	22.24
30	11.86	23.22	2.48	3.79	0.06	0.69	14.40	27.21	11.96	22.56
31	11.90	23.24	2.48	3.79	0.06	0.69	14.44	27.23	11.98	22.55

Please cite this article in press as: Montero, G. et al., Solar radiation and shadow modelling with adaptive triangular meshes, Sol. Energy (2009), doi:10.1016/j.solener.2009.01.004

tional data were also daily mean values. Table 2 contains the daily average and maximum radiation components in December 2006. The average values have been calculated from the results obtained in the whole region. There we observe that beam, diffuse and reflected radiation values are about 82–83%, 16–17% and 0–0.4% of the mean global radiation obtained by the model under clear-sky, respectively. Also note that clear-sky radiation is corrected with the observational data. This fact was much more appreciable in that month (winter), where the correction on some overcast days reduced the clear-sky results from 20% to approximately 70%.

The maximum values of global radiation for clear-sky and real-sky, respectively, do not have to be relative to the same location. The effect of the interpolation will produce a smoothing of results where we have not measurement stations. In particular, this is what happens in the case of points of maximum value of radiation. However, this does not imply that we cannot have a clear sky in other zones of the Island. For example, the clear-sky index distributions for days 18 and 27 of December correspond to an overcast day (K_c between 0.24 and 0.37) and clear-sky day (K_c between 0.4 and 1), respectively.

Thus, the description and implementation of the extent of cloud cover in an episode will be essential to apply this model in predictive simulations. In other month (e.g., April), such correction is much less considerable (about 1% on cloudless days and reaching a 30% on overcast days).

Finally, these daily data were added up to yield the monthly maps of the different radiation components and both clear-sky and real-sky global radiations (see Figs. 8–12) of December 2006. The information of stations C1 and C5 results in a considerable correction of the global solar radiation in the North-East of the island. It is well known that this local phenomenon often occurs in that zone. The impact of the terrain on the radiation field should, in the Northern hemisphere (above the Tropic) result in a decrease in radiation sums on the north facing slopes and an increase in the south facing slopes. However, we have to take the form of the mountains into account. In effect, if we observe the elevation map of Gran Canaria Island, we can see that the contour line at the top of the island has the same angle as the solar maps and the north facing slopes are behind this inclined line.

A similar procedure has been used to obtain the radiation maps of the other months. Table 3 includes the monthly average and maximum radiation components.

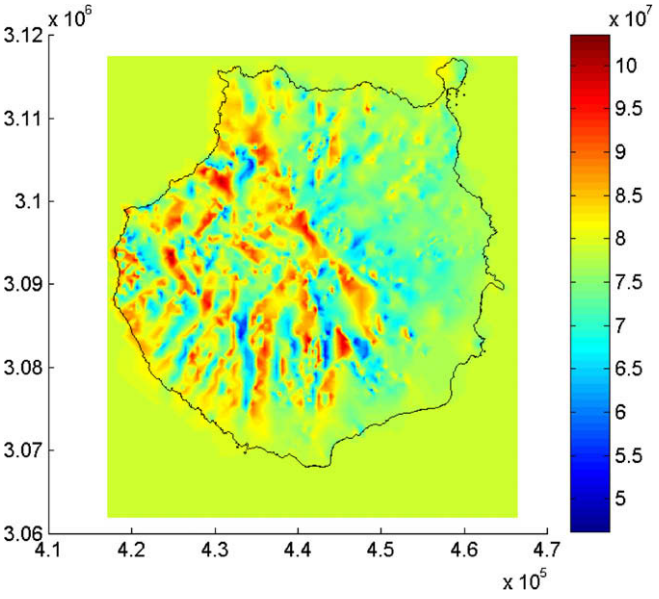

Fig. 9. Diffuse radiation map (J/m^2) relative to December 2006.

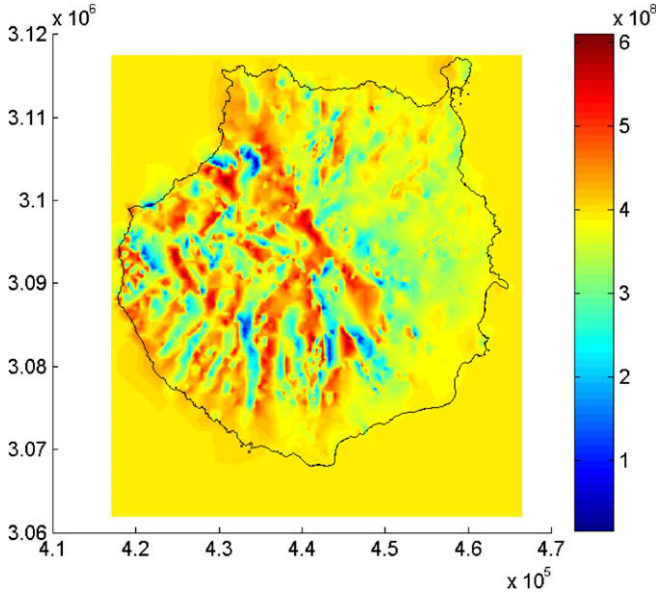

Fig. 8. Beam radiation map (J/m^2) relative to December 2006.

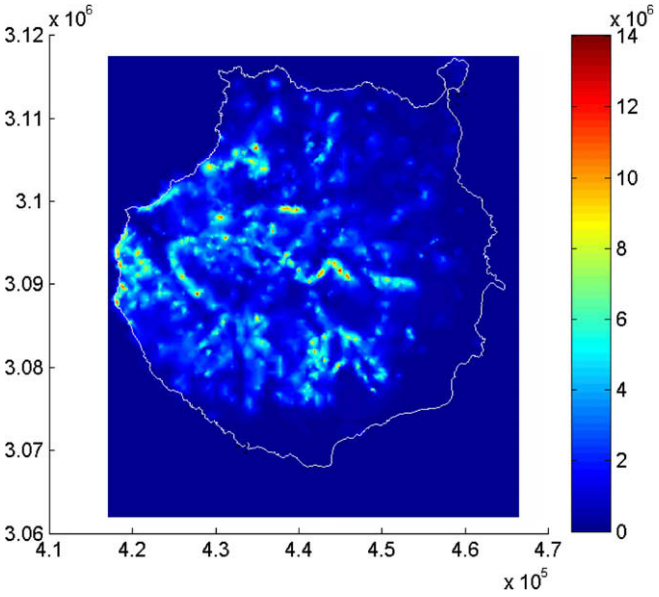

Fig. 10. Reflected radiation map (J/m^2) relative to December 2006.

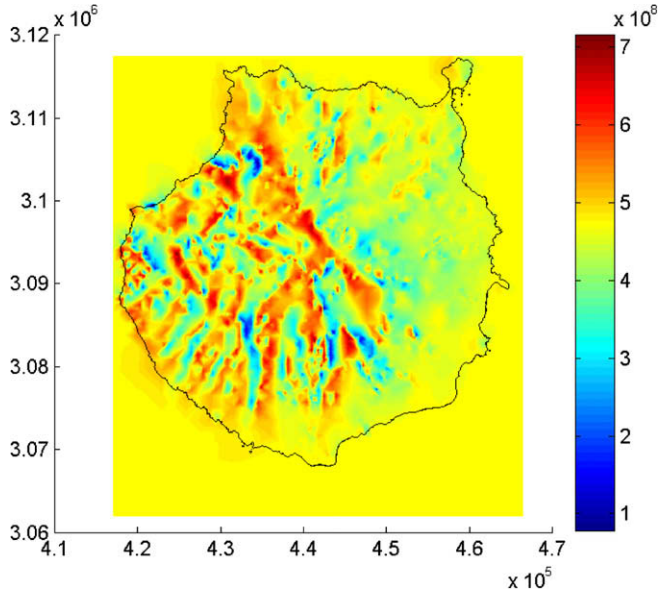

Fig. 11. Clear-sky global radiation map (J/m^2) relative to December 2006.

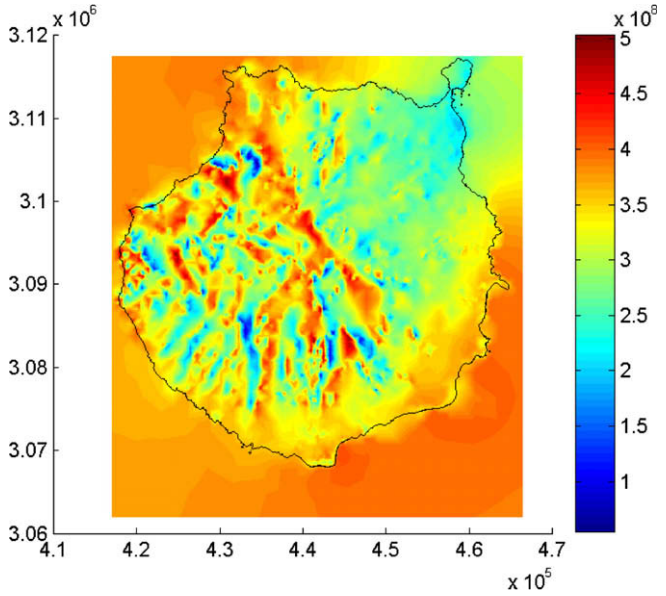

Fig. 12. Real-sky global radiation map (J/m^2) relative to December 2006.

The average real-sky global radiation, considering the 273 days with observational data, is 16.89 MJ/m^2 per day. This result coincides with that of most of the references including radiation data for the Canary Islands (Censolar, 2007; AEMET, 2008; ASDC, 2008; Huld and Suri, 2001–2007; Betcke et al., 2006).

In order to study the effect of shadowing in the solar radiation calculation, we applied the model without shadow information to the episode of December 2006. It evidently resulted in an overestimation of all the components of the solar radiation. By way of example, Fig. 13 illustrates the global clear-sky radiation obtained. A summary of average and maximum values of each radiation component can be seen in the first row of Table 4. An overestimation about 7% in clear-sky beam radiation is obtained in relation to the results of the fine mesh represented in Fig. 16.

We also applied the model to the same case using other meshes, more specifically, one coarse mesh, one fine mesh and finally one regular mesh of about the same number of nodes as the initial mesh in Fig. 7. For the coarse mesh, we used $\varepsilon_h = 240$ and $\varepsilon_a = 0.10$, obtaining a mesh with 2164 nodes and 4247 triangles. This mesh is represented in Fig. 14. The regular mesh (see Fig. 15) was built without considering any refinement/derefinament parameter, obtaining a mesh with 5913 nodes and 11,520 triangles. Finally, the fine mesh in Fig. 16, containing 9276 nodes and 18,462 triangles, was constructed with $\varepsilon_h = 100$ and $\varepsilon_a = 0.07$.

The results of clear-sky global radiation are shown in Figs. 17–19, respectively. Similar conclusions to those of Cebecauer et al. (2007) are drawn, since resolutions for $\varepsilon_h > 200$ m (coarse mesh) may produce local overestimation of solar radiation. The regular mesh (with a resolution of 677 m approximately) also produced an overestimation of the radiation (Cebecauer et al., 2007 conclude an overestimation of solar radiation for resolutions greater than 500 m). The correction (decreasing) of the radiation in finer

Table 3
Monthly average and maximum beam, diffuse, reflected clear-sky radiations. Also clear-sky and real-sky global radiations are included. All of them are represented in MJ/m^2.

Month	Clear-sky								Real-sky	
	Beam rad.		Diffuse rad.		Reflected rad.		Global rad.		Global rad.	
	Aver.	Max.	Aver.	Max.	Aver.	Max.	Aver.	Max.	Aver.	Max.
September 2006	597.32	726.97	117.21	129.14	3.08	34.01	717.61	861.41	592.93	711.97
October 2006	500.22	705.89	104.74	127.98	2.59	29.17	607.56	845.09	485.87	676.95
November 2006	402.81	700.54	85.28	120.03	2.04	23.73	490.13	827.37	318.38	535.22
December 2006	369.54	719.85	76.85	117.30	1.83	21.37	448.22	843.41	314.70	586.25
January 2007	423.19	776.62	69.62	104.26	2.04	23.79	494.85	887.76	374.45	677.80
February 2007	478.73	732.72	68.44	91.35	2.30	26.23	549.47	831.64	467.95	709.14
March 2007	623.56	795.44	98.48	113.72	3.09	34.35	725.13	915.68	612.34	775.65
April 2007	684.81	786.35	110.76	118.78	3.46	37.58	799.03	905.13	703.66	791.67
May 2007	732.71	823.18	130.52	137.10	3.77	41.79	867.01	957.64	740.27	817.83

Please cite this article in press as: Montero, G. et al., Solar radiation and shadow modelling with adaptive triangular meshes, Sol. Energy (2009), doi:10.1016/j.solener.2009.01.004

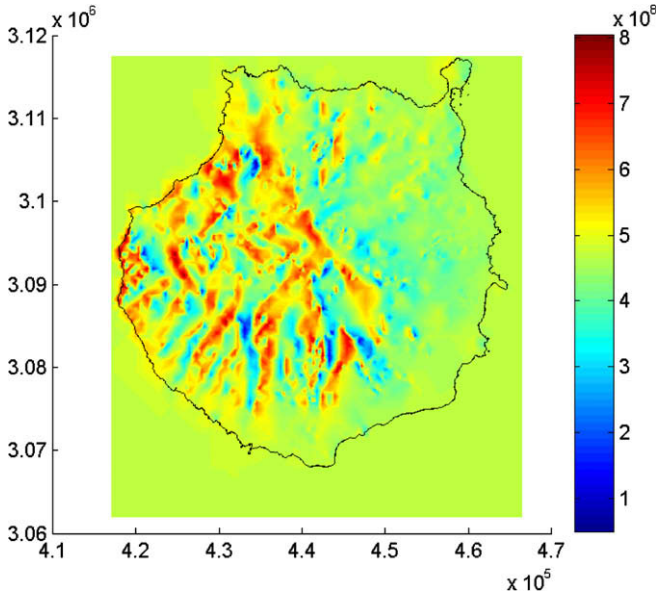

Fig. 13. Clear-sky global radiation map (J/m^2) relative to December 2006 without shadow detection.

meshes is stabilized with the local refinement. For example, the overestimation of beam radiation for the regular, coarse and intermediate meshes with respect to the finer mesh are 7.4%, 5.5% and 1,9%, respectively; see Table 4. We note that even the coarse mesh provides better results than the regular one if we consider average values. However, the number of nodes of the former is almost one third that of the latter.

Other authors such as McKenney et al. (1999) have studied the differences in the solar radiation estimates with a spatially distributed solar radiation model (SRAD), using different DEM (Digital Elevation Model) resolutions. Once again the main advantage of our approach is the possibility of using adaptive meshes, thus obtaining better results at a lower computational cost.

6. Conclusions

A numerical model for estimating the solar radiation on a surface is proposed. The requirements for a simulation are the location, topography, albedo and observational data. Then, defining the limits of the episode to be simulated, the solar radiation on a surface is estimated taking into account the shadow distribution in each time step. For this purpose, the adaptivity of the triangulation related to the topography and albedo is essential in order to obtain accurate results of shadow distribution and also of solar radiation. Adaptive meshes lead to a minimum computational cost, since the number of triangles to be used is optimum.

The accuracy of the model results depends on the number of points for which we have realistic data. In effect, the quality of the real-sky component of the model is directly related to the observational information. One aspect to be improved in future works is the interpolation procedure used for processing such data. The proposed interpolation method is suitable, when a considerable number of stations are available and they are well distributed in the zone under study since this tends to smooth out extremes. Moreover, in such cases, one can think about using more sophisticated techniques, such as spline functions for interpolating the clear-sky index on the surface (see e.g., Xia et al. (2000)) or moving least-square approximation as used in meshless methods (Belytschko et al., 1996). Another possibility is to add meteorological information (for example, from MM5, WRF, HIRLAM) to draw the map of clear-sky index.

Some unknown parameters of the model, whose values are not clear a priori, may be estimated using genetic algorithms to minimize the error between the measures and the results of the model in the observational points. This is the case of parameter epsilon in Eq. (38). A similar problem was solved in a wind model with the same interpolation formulae in Montero et al. (2005).

To include rectangular collectors in the model is not difficult, if we consider each collector as composed by two triangles in the same plane. The steps to be followed with these triangles are the same as those developed for the rest of triangles of the mesh. Therefore, the problem would be reduced to the analysis of the solar radiation on such triangles for a given inclination angle of the southwards-oriented collectors. In this case, even shadows induced by the collectors can be considered. Moreover, we think that this model could be used to calculate the optimal orientation and inclination of solar collectors for each location.

Further research is needed in the optimal selection of the warning points for detecting the shadows. On the other hand, the boundary of the shadows may be accurately determined using the refinement/derefinement procedure

Table 4
Average and maximum beam, diffuse, reflected clear-sky radiations in December 2006 after different strategies of shadowing and meshing. Also clear-sky and real-sky global radiations are included. All of them are represented in MJ/m^2.

Strategy	Clear-sky								Real-sky	
	Beam rad.		Diffuse rad.		Reflected rad.		Global rad.		Global rad.	
	Aver.	Max.	Aver.	Max.	Aver.	Max.	Aver.	Max.	Aver.	Max.
No shadow detection	387.90	754.32	76.79	120.36	2.01	24.01	466.71	891.51	322.71	614.04
Regular mesh	389.47	658.99	78.28	108.27	0.61	12.75	468.36	771.91	329.99	551.25
Coarse mesh	382.47	680.57	77.41	108.84	0.87	17.62	460.75	797.75	320.62	536.08
Intermediate mesh	369.54	719.85	76.85	117.30	1.83	21.37	448.22	843.41	314.70	586.25
Fine mesh	362.65	725.40	76.56	115.10	2.29	26.09	441.50	849.78	312.82	601.23

Please cite this article in press as: Montero, G. et al., Solar radiation and shadow modelling with adaptive triangular meshes, Sol. Energy (2009), doi:10.1016/j.solener.2009.01.004

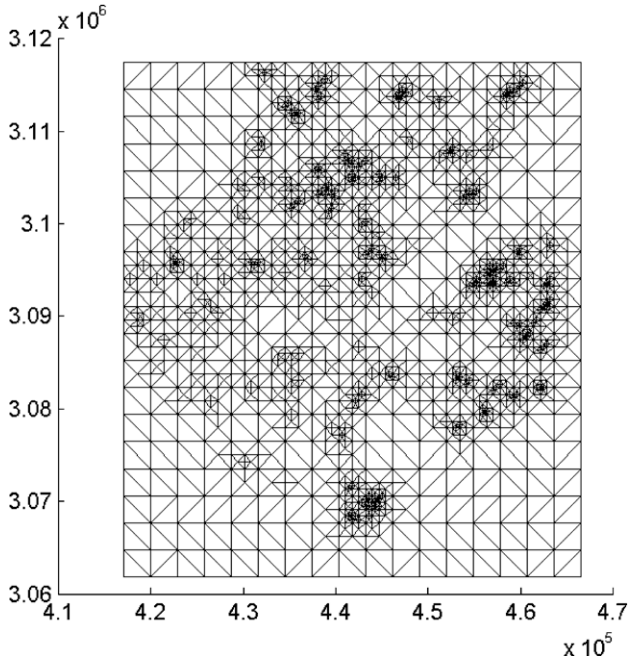

Fig. 14. Coarser triangular mesh adapted to topography and albedo.

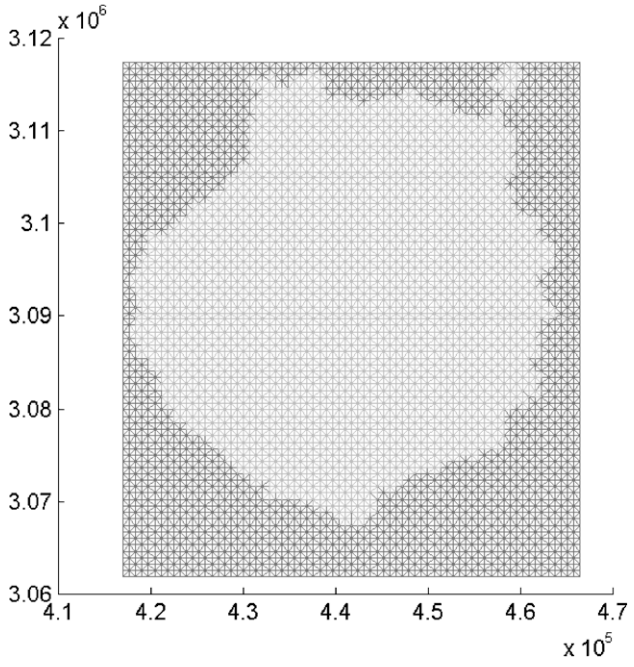

Fig. 15. Regular triangular mesh adapted to topography and albedo.

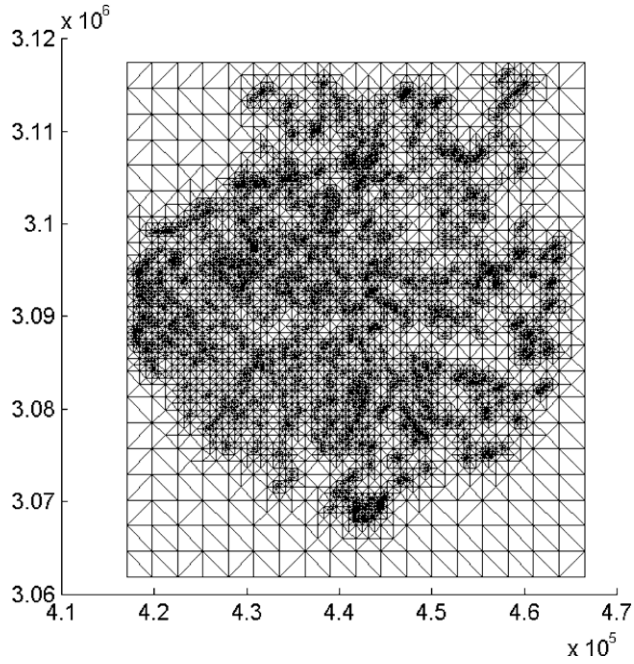

Fig. 16. Finer triangular mesh adapted to topography and albedo.

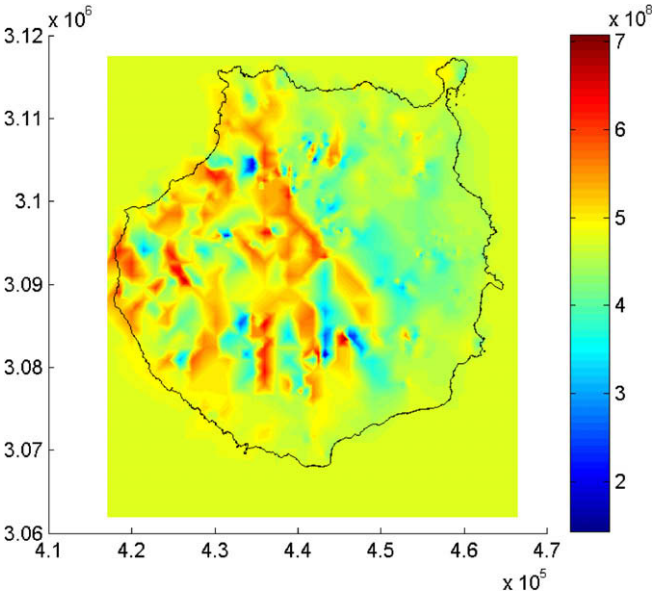

Fig. 17. Clear-sky global radiation map (J/m^2) relative to December 2006 with a coarser mesh.

and mesh adaption by moving nodes to such contour line. A possible solution is to refine those triangles where $0 < L_f < 1$. The first idea is to connect the number of warning points with the size of the triangle (which is equivalent to a consecutive refining by using 4-T Rivara's algorithm) by placing the warning points in the geometrical centre of the respective resulting triangles, as it was indicated in Section 3. If we use a different adaptive mesh in each time step, a simple strategy can be to start from the mesh of the previous time step and to apply the refinement/derefinement algorithm considering the new solar position. Finally, we should use a reference regular mesh in order to calculate the mean daily radiation values.

Also, any standard error indicator may be defined for each triangle in order to refine/derefine the mesh attending to the daily numerical solution of the real-sky global radiation. The change of the sky dome fraction due to the presence of terrain sky line should be considered as well. Finally, since the evaluation of all the radiation components in any triangle is independent from each other, their

Please cite this article in press as: Montero, G. et al., Solar radiation and shadow modelling with adaptive triangular meshes, Sol. Energy (2009), doi:10.1016/j.solener.2009.01.004

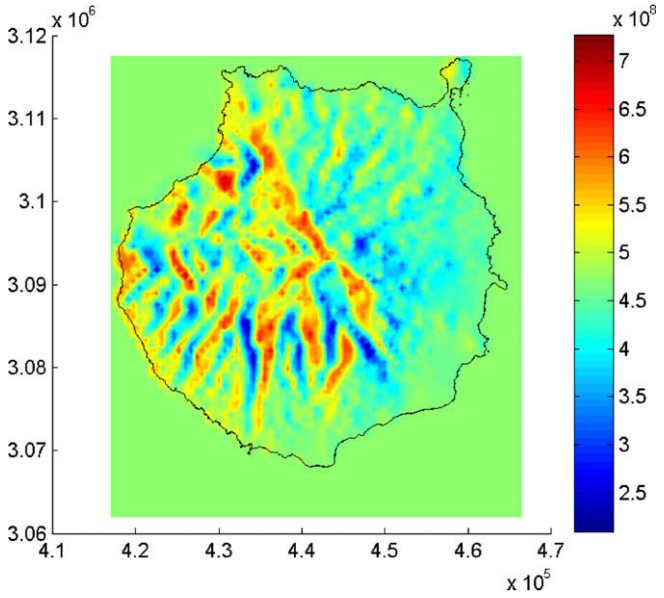

Fig. 18. Clear-sky global radiation map (J/m^2) relative to December 2006 with a regular mesh.

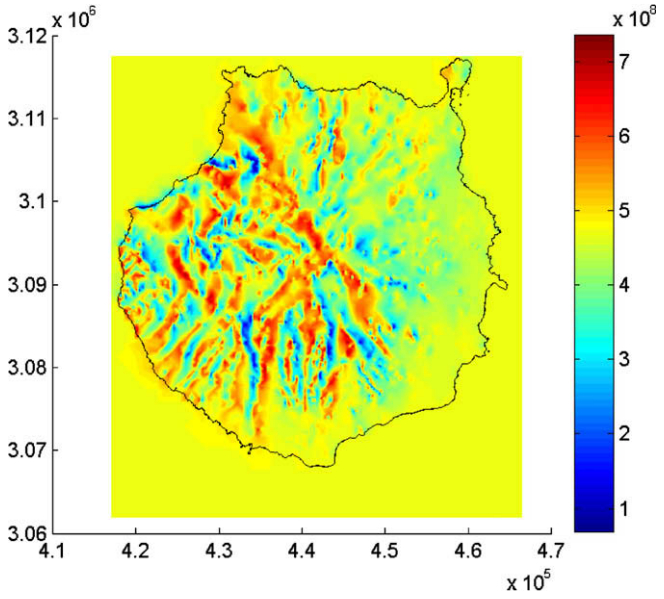

Fig. 19. Clear-sky global radiation map (J/m^2) relative to December 2006 with a finer mesh.

calculation may be fully parallelized, which would reduce the computational cost considerably.

Acknowledgments

This work has been supported by the *Dirección General de Investigación*, *Ministerio de Educación y Ciencia*, Spanish Government, Grant contract CGL2007-65680-C03-01/CLI and the *Dirección General de Investigación*, *Ministerio de Ciencia e Innovación*, Spanish Government, Grant contract CGL2008-06003-C03-01/CLI. The authors are grateful to Antonio Ortegón Gallego of the Canary Islands Technological Institute for providing them with the observational data of solar radiation in its stations for three months of the episode under study. Finally, the authors wish to express their sincere thanks to the three anonymous reviewers, whose comments and suggestions were very helpful.

References

Agencia Estatal de Meteorología of the Spanish Government (AEMET), 2008. Available from: <http://www.ae-met.es/es/portada>.

Atmospheric Science Data Center, 2008. Surface meteorology and Solar Energy. Available from: <http://eosweb.larc.nasa.gov/sse/>.

Belytschko, T., Krongauz, Y., Organ, D., Fleming, M., Krysl, P., 1996. Meshless methods: an overview and recent developments. Computer Methods in Applied Mechanics and Engineering 139, 3–47.

Betcke, J., Kuhlemann, R., Hammer, A., Drews, A., Lorenz, E., Girodo, M., Heinemann, D., Wald, L., Cros, S., Schroedter-Homscheidt, M., Holzer-Popp, Th., Gesell, G., Erbertseder, Th., Kosmale, M., Hildenbrand, B., Dagestad, K.F., Olseth, J., Ineichen, P., Reise, Ch., Dumortier, D., van Roy, F., Ortegon, A., Beyer, H.G., Trieb, F., Schillings, Ch., Hoyer, C., Kronshage, S., Mannstein, H., Bugliaro, L., Krebs, W., 2006. Energy-specific Solar Radiation Data from Meteosat Second Generation (MSG): The Heliosat-3 Project. Final Report. European Commission, Community Research, Energy, Environment and Sustainable Development.

Cebecauer, T., Huld, T., Súri, M., 2007. Using high-resolution digital elevation model for improved PV yield estimates. In: Proceedings of the 22nd European Photovoltaic Solar Energy Conference, Milano, Italy, pp. 3553–3557.

Censolar (Centros de Estudios de la Energía Solar), 2007. Distribución horaria de la irradiación solar global incidente sobre superficie horizontal en las cinco zonas climáticas definidas en el Código Técnico de la Edificación de España. Technical Report. Available from: <http://www.asif.org/files/Distribucion_horaria_-irradiancia_solar_v-zonas_CTEEsp.pdf> (in Spanish).

Cogliani, E., Ricchiazzi, P., Maccari, A., 2008. Generation of operational maps of global solar irradiation on horizontal plan and of direct normal irradiation from Meteosat imagery by using SOLARMET. Solar Energy 82 (6), 556–562.

Cucumo, M., Kaliakatsos, D., Marinelli, V., 2000. A calculation method for the estimation of the Linke turbidity factor. Renewable Energy 19 (1–2), 249–258.

Diabaté, L., Remund, J., Wald, L., 2003. Linke turbidity factors for several sites in Africa. Solar Energy 75 (2), 111–119.

Dozier, J., Bruno, J., Downey, P., 1981. A faster solution to the horizon problem. Computers & Geosciences 7, 145–151.

Ferragut, L., Montenegro, R., Plaza, A., 1994. Efficient refinement/derefinement algorithm of nested meshes to solve evolution problems. Communications in Numerical Methods in Engineering 10, 403–412.

Gruter, J.W. (Ed.) 1984. Radiation Nomenclature. Brussels, CEC, Second Solar Energy Programme, Project F, Solar Radiation Data.

Huld, T., Suri, M., 2001–2007. PVGIS PV Estimation Utility. Institute for Environment and Sustainability (IES). Available from: <http://sunbird.jrc.it/pvgis/apps-/pvest.php?lang=en&map=africa&app=gridcon-nected>.

Jenčo, M., 1992. Distribúcia priameho slnecného iarenia na georeliéfe a jej modelovanie pomocou komplexného digitálneho modelu georeliéfu. Geografický casopis 44 (4), 342–354.

Kasten, F., 1996. The Linke turbidity factor based on improved values of the integral Rayleigh optical thickness. Solar Energy 56 (3), 239–244.

Kasten, F., Young, A.T., 1989. Revised optical air mass tables and approximation formula. Applied Optics 28, 4735–4738.

Krcho, J., 1990. Morfometrická analýza a digitálne modely georeliéfu. Veda, Bratislava.

Kuhlemann, R., Hammer, A., Drews, A., 2005. Geolocation of High Resolution Data of Meteosat-8 (VCS-XPIF format). Technical Report. Energy-specific Solar Radiation Data from Meteosat Second

Generation (MSG): The Heliosat-3 Project. European Commission, Community Research, Energy, Environment and Sustainable Development.

McKenney, D.W., McKey, B.G., Zavitz, B.L., 1999. Calibration and sensitivity analysis of a spatially-distributed solar radiation model. International Journal of Geographical Information Science 13 (1), 49–65.

Montenegro, R., Montero, G., Escobar, J.M., Rodríguez, E., 2002a. Efficient strategies for adaptive 3-D mesh generation over complex orography. Neural, Parallel and Scientific Computations 10 (1), 57–76.

Montenegro, R., Montero, G., Escobar, J.M., Rodríguez, E., González-Yuste, J.M., 2002b. Tetrahedral mesh generation for environmental problems over complex terrains. Lecture Notes in Computer Science 2329, 335–344.

Montero, G., Montenegro, R., Escobar, J.M., 1998. A 3-D diagnostic model for wind field adjustment. Journal of Wind Engineering and Industrial Aerodynamics 74–76, 249–261.

Montero, G., Montenegro, R., Escobar, J.M., Rodríguez, E., 2003. Generación automática de mallas de tetraedros adaptadas a orografías irregulares. Revista Internacional de Métodos Numéricos para Cálculo y Diseño en Ingeniería 19 (2), 127–144.

Montero, G., Montenegro, R., Escobar, J.M., Rodríguez, E., González-Yuste, J.M., 2004. Velocity field modelling for pollutant plume using 3-D adaptive finite element method. Lecture Notes in Computer Science 3037, 642–645.

Montero, G., Rodríguez, E., Montenegro, R., Escobar, J.M., González-Yuste, J.M., 2005. Genetic algorithms for an improved parameter estimation with local refinement of tetrahedral meshes in a wind model. Advances in Engineering Software 36, 3–10.

Muneer, T., 1990. Solar radiation model for Europe. Building Services Engineering Research and Technology 11, 153–163.

Muneer, T., 1997. Solar Radiation and Daylight Models for Energy Efficient Design of Buildings. Architectural Press, Oxford.

Niewienda, A., Heidt, F.D., 1996. SOMBRERO: a PC-tool to calculate shadows on arbitrarily oriented surfaces. Solar Energy 58 (4–6), 253–263.

Page, J.K. (Ed.), 1986. Prediction of Solar Radiation on Inclined Surfaces. D. Reidel Publishing Co., Dordrecht.

Plaza, A., Montenegro, R., Ferragut, L., 1996. An improved derefinement algorithm of nested meshes. Advances in Engineering Software 27 (1–2), 51–57.

Rivara, M.C., 1987. A grid generator based on 4-triangles conforming. Mesh-refinement algorithms. International Journal for Numerical Methods in Engineering 24, 1343–1354.

Scharmer, K., Greif, J., 2000. The European Solar Radiation Atlas. Database and Exploitation Software, vol. 2. Les Presses de l'École des Mines, Paris.

Şen, Z., Şahin, A.D., 2001. Spatial interpolation and estimation of solar irradiation by cumulative semivariograms. Solar Energy 71 (1), 11–21.

SoDa Service (Solar Data), 2004–2007. Services for Professionals in Solar Energy and Radiation. Available from: <http://www.soda-is.com/eng/services/service_in-voke/gui.php>.

Stewart, A.J., 1998. Fast horizon computation at all points of a terrain with visibility and shading applications. IEEE Transactions on Visualization and Computer Graphics 4 (1), 82–93.

Šúri, M., Hofierka, J., 2002. The solar radiation model for Open source GIS: implementation and applications. In: Benciolini, B., Ciolli, M., Zatelli, P. (Eds.), Proceedings of the Open Source GIS-GRASS Users Conference, Trento, Italy, pp. 1–19.

Šúri, M., Hofierka, J., 2004. A new GIS-based solar radiation model and its application to photovoltaic assessments. Transactions in GIS 8 (2), 175–190.

Winter, G., Montero, G., Ferragut, L., Montenegro, R., 1995. Adaptive strategies using standard and mixed finite element for wind field adjustment. Solar Energy 54 (1), 46–56.

Xia, Y., Winterhalter, M., Fabian, P., 2000. Interpolation of daily global solar radiation with thin plate smoothing splines. Theoretical and Applied Climatology 66, 109–115.

Zakey, A.S., Abdelwahab, M.M., Makar, P.A., 2004. Atmospheric turbidity over Egypt. Atmospheric Environment 38 (11), 1579–1591.

Zakšek, K., Podobnikar, T., Oštir, K., 2005. Solar radiation modelling. Computers & Geosciences 31 (2), 233–240.

Please cite this article in press as: Montero, G. et al., Solar radiation and shadow modelling with adaptive triangular meshes, Sol. Energy (2009), doi:10.1016/j.solener.2009.01.004